日本磁気学会
ISSN 2432-0250
Journal of the Magnetics Society of Japan
Electronic Journal URL: https://www.jstage.jst.go.jp/browse/msjmag

Vol.48 No.5　2024

Journal

JOURNAL OF THE MAGNETICS SOCIETY OF JAPAN

Vol.48 No.5 2024

日本磁気学会

ISSN 2432-0250

HP: http://www.magnetics.jp/ e-mail: msj@bj.wakwak.com

Electronic Journal: http://www.jstage.jst.go.jp/browse/msjmag

TPM-2-08s25

HcJの3σ/Ave. 0.2%※1を実現

渦電流補正方法※2も確立済

試料測定磁界 max 15Tesla

最大試料直径 10mm

パルス励磁型磁気特性測定装置

永久磁石および磁性体粉末を固形化した高磁化試料のヒステリシス曲線の自動測定および描画、SPD（Singuler Point Detection）測定が可能です。（RT～+200℃）

※1　電気学会資料 MAG-18-088 参照

※2　電気学会資料 MAG-07-011 参照

NdFeB(sintered) 測定例

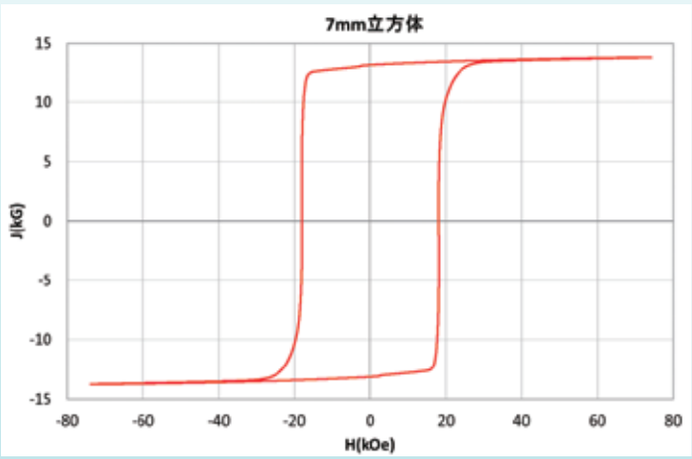

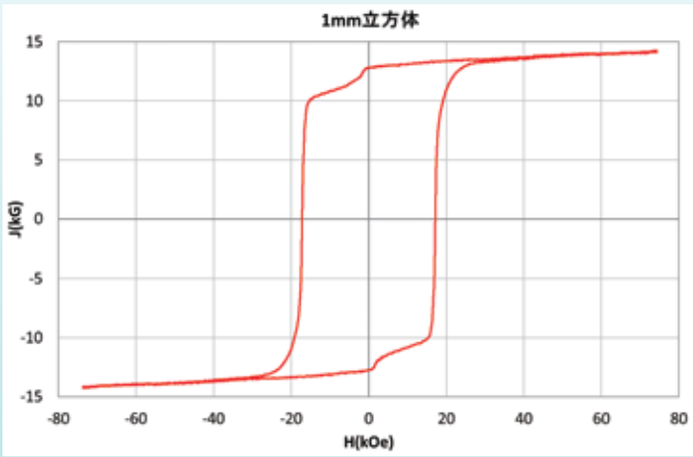

1mm 立方体測定用検出コイルはオプション品です

東英工業では他に振動試料型磁力計(VSM)、直流自記磁束計(JIS C2501 準拠)を始め、

各種磁気測定装置を取り揃えております。ぜひお問い合わせ下さい

東英工業株式会社
http://www.toeikogyo.co.jp

〒194-0035 東京都町田市忠生1-8-13
TEL：042-791-1211 FAX：042-792-0490
E-mail：sales@toeikogyo.co.jp

Journal of the Magnetics Society of Japan
Vol. 48, No. 5

Electronic Journal URL: https://www.jstage.jst.go.jp/browse/msjmag

CONTENTS

J. Magn. Soc. Jpn., **48**, 81-87 (2024) <Paper>

Influence of Anisotropy Constant on Writability in Heated-Dot Magnetic Recording

T. Kobayashi, Y. Nakatani*, and I. Tagawa**

Graduate School of Engineering, Mie Univ., *1577 Kurimamachiya-cho, Tsu 514-8507, Japan*

*Graduate School of Informatics and Engineering, Univ. of Electro-Communications, *1-5-1 Chofugaoka, Chofu 182-8585, Japan*

**Electrical and Electronic Engineering, Tohoku Institute of Technology, *35-1 Yagiyama-Kasumicho, Sendai 982-8577, Japan*

We discuss the influence of the anisotropy constant on writability, taking account of 10 years of archiving and adjacent track interference in 4 Tbpsi shingled heated-dot magnetic recording (HDMR), using our stochastic calculation employing the Néel-Arrhenius model with a Stoner-Wohlfarth dot. The bit error rate is calculated and the result is analyzed using the mean magnetization reversal number per unit time as a function of the writing time. We confirm the stochastic calculation result by employing a micromagnetic simulation. HDMR has a certain margin for erasure-after-write, since half of the writing time determined by field is for the magnetic dot and the rest is for the nonmagnetic spacing. HDMR also has a certain margin for the dot aspect ratio, since the dot is relatively large. Therefore, the combination of a small anisotropy constant and a large dot volume can be used to improve write-error. When we choose a small anisotropy constant, the mean magnetization reversal number per unit time in the opposite direction to the recording direction is negligible. Furthermore, the writing time determined by medium is longer. Therefore, the bit error rate caused by write-error is low for a small anisotropy constant.

Key words: HDMR, 10 years of archiving, ATI, dot height, bit error rate, anisotropy constant ratio

1. Introduction

Many magnetic recording methods have been proposed to solve the trilemma problem[1] of conventional magnetic recording (CMR) on granular media. These methods include shingled magnetic recording (SMR), microwave-assisted magnetic recording (MAMR), heat-assisted magnetic recording (HAMR), bit patterned media (BPM), heated-dot magnetic recording (HDMR), namely HAMR on BPM, and three-dimensional magnetic recording (3D MR).

The challenges to be faced when designing MR media are

(1) information stability during 10 years of archiving, known as the $K_uV/(kT)$ problem[1], where K_u, V, k, and T are, respectively, the grain or dot anisotropy constant, volume, the Boltzmann constant, and temperature,

(2) information stability in an adjacent track (AT) during writing, known as the adjacent track interference (ATI) problem, and

(3) the writing field dependence of the bit error rate (bER), namely writability.

Akagi *et al.* reported (3) the recording performance of HDMR[2] and 3D HDMR[3,4] employing micromagnetic simulation. They assumed the medium material to be FePt. However, the K_u value was smaller than that of bulk FePt.

The above three challenges, namely (1), (2), and (3), must be dealt with simultaneously, since they are in a trade-off relationship. If a small K_u value is chosen, the information stabilities in (1) and (2) will be worse.

Corresponding author: T. Kobayashi (e-mail: kobayasi @phen.mie-u.ac.jp).

In this paper, we discuss the influence of K_u on (3) writability, taking account of (1) 10 years of archiving and (2) ATI in 4 Tbpsi shingled HDMR, using our stochastic calculation employing the Néel-Arrhenius model with a Stoner-Wohlfarth dot. We confirm the stochastic calculation result by employing a micromagnetic simulation. Our calculation is applicable to all three challenges[5] including SMR and CMR. The anisotropy constant ratio K_u/K_{bulk}, which we introduced[6,7], is used instead of K_u. The K_u/K_{bulk} value is the intrinsic ratio of the medium K_u to the bulk FePt K_u. Therefore, it becomes easy to grasp the ratio to the bulk K_u. If we employ K_u/K_{bulk}, we can choose a reasonable K_u value for the medium. For example, although we can choose a K_u value of 60 Merg/cm^3 at 300 K for a medium with a T_c value of 750 K since the K_u/K_{bulk} value is less than 1.0, that of 70 Merg/cm^3 cannot be selected since the K_u/K_{bulk} value exceeds 1.0 as reported in a previous paper[7].

2. Calculation Conditions and Method

2.1 Dot arrangement and medium structure

Figure 1 shows the dot arrangement and medium structure in 4 Tbpsi HDMR where D_x, D_y, and h are the dot sizes for the down-track x and cross-track y directions, and the dot height, respectively. The z direction is film normal. The bit length D_B and track width D_T are both 12.7 nm. We assume that the mean dot size D_m and mean dot spacing Δ_D are the same for both the down-track and cross-track directions, namely $D_m = \Delta_D = 6.35$ nm.

There are two cases as regards the dot sizes D_x and D_y depending on the dot manufacturing method. In one case, the D_x and D_y sizes are the same, and the $D_x =$

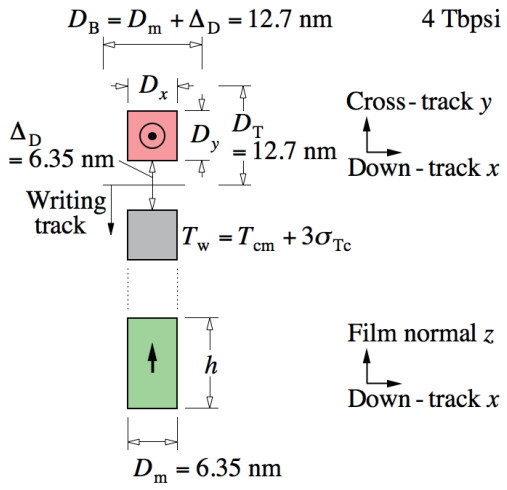

Fig. 1 Dot arrangement and medium structure.

D_y size fluctuates. In the other case, the D_x and D_y sizes fluctuate independently. We examined the $D_x = D_y$ case, since the bER is larger for the same h value[8]. We generated a random number $D_x = D_y$ that had a log-normal distribution with a standard deviation σ_D. We used a σ_D/D_m value of 15 %.

2.2 Magnetic properties

The temperature dependence of the medium magnetization M_s was calculated by employing mean field analysis[9], and that of the K_u value was assumed to be proportional to M_s^2[10]. $M_s(T_c = 770\ \mathrm{K}, T = 300\ \mathrm{K}) = 1000$ emu /cm^3 was assumed for FePt. Based on this assumption, the M_s value can be calculated for all values of T_c and T.

$K_u(T_c = 770\ \mathrm{K}, K_u/K_{bulk} = 1, T = 300\ \mathrm{K}) = 70$ Merg/cm^3 was assumed for bulk FePt. Using this assumption, we can calculate K_u for all values of T_c, K_u/K_{bulk}, and T. No intrinsic distribution of K_u was assumed. However, there was a fluctuation in K_u caused by T_c variation.

Since each dot has a T_c variation, the T_c value of each dot was adjusted by changing the Cu composition c for $(Fe_{0.5}Pt_{0.5})_{1-c}Cu_c$.

With a T_c value of 750 K and a K_u/K_{bulk} value of 0.8, in this work we obtain a K_u value of 51 Merg/cm^3 and an anisotropy field H_k of 107 kOe at a readout temperature of 330 K employing mean field analysis.

2.3 Temperature profile and writing field

The writing temperature T_w for the dot was assumed to be

$$T_w = T_{cm} + 3\sigma_{Tc}, \qquad (1)$$

as shown in Fig. 1, taking account of the T_c variation, where T_{cm} and σ_{Tc} are the mean Curie temperature and the standard deviation of T_{cm}, respectively. The T_c distribution was assumed to be normal. Based on this assumption, 99.9 % of dots in the writing track are heated to above their T_c values during the writing period. We used T_{cm} and σ_{Tc}/T_{cm} values of 750 K and 2 %, respectively.

For simplicity, we used a thermal gradient $\partial T/\partial y$ of 14 K/nm in the cross-track direction and assumed it to be constant anywhere for ATI. A constant $\partial T/\partial x$ value of 14 K/nm in the down-track direction was also used for writability.

The writing field H_w was assumed to be spatially uniform, the direction to be perpendicular to the medium plane, and the rise time to be zero.

2.4 Stochastic calculation method

The information stability for 10 years of archiving has been discussed employing the Néel-Arrhenius model with a Stoner-Wohlfarth grain or dot. The attempt period $1/f_\alpha$ has a value of picoseconds for FePt in heat-assisted magnetic recording. Since the magnetization direction attempts to reverse with a certain probability at each attempt period, the information stability for 10 years of archiving is extrapolated as a stack of phenomena in picoseconds. Therefore, the Néel-Arrhenius model is valid for any time from the order of a picosecond to more than 10 years. The Néel-Arrhenius model is also valid under the condition that the writing field is less than the anisotropy field of recording media. Not only in ATI but in writability, the anisotropy field is larger than the writing field during most of the writing time, since the anisotropy field of FePt is extremely large. In HAMR including HDMR, stochastic magnetization switching under thermal agitation is dominant even for writability. Therefore, we have also applied the Néel-Arrhenius model to phenomena with a short time, and examined ATI[8,11] and writability[7].

The three challenges, 10 years of archiving, ATI, and writability, must be dealt with simultaneously. Therefore, in this paper we discuss the influence of K_u on writability for HDMR, taking account of 10 years of archiving and ATI. The results for 10 years of archiving[8] and ATI[8,11] have already been reported. The criterion determining whether or not information is stable after 10 years of archiving and AT writing was assumed to be a bER of 10^{-3}.

We improved our stochastic calculation for writability. We first took the shape anisotropy reported in a previous paper[12] into account. The magnetostatic field from surrounding dots was ignored since the Δ_D value is large. Then we modified the attempt frequency f_α as described below.

We assumed f_α as

$$f_\alpha = \frac{\gamma\alpha}{1+\alpha^2}\sqrt{\frac{M_s H_{keff}^3 V}{2\pi kT}}\left(1-\left(\frac{|H_w|\cos\phi}{(K_u/K_{bulk})H_{const}}\right)^2\right)\left(1+\frac{|H_w|\cos\phi}{(K_u/K_{bulk})H_{const}}\right), \qquad (2)$$

taking account of an approximation[13], where γ, α, H_{keff}, $|H_w|$, and ϕ are the gyromagnetic ratio, Gilbert damping constant, effective anisotropy field, writing

field magnitude, and writing field angle, respectively. We used γ and α values of 1.76×10^{7} $Oe^{-1}s^{-1}$ and 0.1, respectively. When ϕ = 180 deg, the magnetization reverses in the recording direction and we defined f_α as $f_{\alpha-}$. When ϕ = 0, the magnetization reverses in the opposite direction to the recording direction and we defined f_α as $f_{\alpha+}$. We introduced $(K_u/K_{bulk})H_{const}$ (H_{const} = 75 kOe) instead of H_{keff} so that the f_α value becomes zero at T_c.

The mean magnetization reversal number N per unit time is expressed as

$$N = f_\alpha \exp(-K_\beta), \tag{3}$$

employing the Néel-Arrhenius model, where K_β is the thermal stability factor. The f_α value gives an attempt number per unit time for magnetization reversal, and the Boltzmann factor $\exp(-K_\beta)$ is interpreted as the probability of magnetization reversal.

When ϕ = 180 deg, namely the magnetization reversal in the recording direction, K_β and N are given by

$$K_{\beta-} = 0 \text{ for } |H_w| \geq H_{keff},$$
$$K_{\beta-} = \frac{K_{ueff}V}{kT}\left(1-\frac{|H_w|}{H_{keff}}\right)^2 \text{ for } |H_w| < H_{keff}, \text{ and} \tag{4}$$

$$N_- = f_{\alpha-} \exp(-K_{\beta-}), \tag{5}$$

respectively, where K_{ueff} is the effective anisotropy constant. And when ϕ = 0, namely the magnetization reversal in the opposite direction to the recording direction, K_β and N are given by

$$K_{\beta+} = \frac{K_{ueff}V}{kT}\left(1+\frac{|H_w|}{H_{keff}}\right)^2, \text{ and} \tag{6}$$

$$N_+ = f_{\alpha+} \exp(-K_{\beta+}), \tag{7}$$

Table 1 Calculation conditions.

Recording density (Tbpsi)	4
Bit length D_B (nm)	12.7
Track width D_T (nm)	12.7
Mean dot size D_m (nm)	6.35
Standard deviation σ_D / D_m (%)	15
Mean dot spacing Δ_D (nm)	6.35
Mean Curie temperature T_{cm} (K)	750
Standard deviation σ_{Tc} / T_{cm} (%)	2
Gilbert damping constant α	0.1
Thermal gradient $\partial T / \partial x$ (K / nm)	14
Linear velocity (m / s)	10
Storage temperature (K) for 10 years of archiving	350
Thermal gradient $\partial T / \partial y$ (K / nm) for ATI	14
Exposure field (kOe) for ATI	10
Exposure time (ns) for ATI	1

respectively.

The calculation procedure for the writing field dependence of the bER, namely writability, is described below. The dot temperature fell with time from T_c according to the linear velocity and $\partial T/\partial x$. The attempt times were calculated using f_α. The probability $\exp(-K_\beta)$ for the magnetization reversal in the recording or opposite direction was calculated for every attempt time. The magnetization direction was determined by the Monte Carlo method for every attempt time. Then the bER value was obtained. The calculation detail has already been reported[7].

The bER in this paper is useful only for comparisons.

The calculation conditions are summarized in Table 1. The linear velocity was 10 m/s. We assumed the storage temperature to be 350 K for 10 years of archiving, for which we took a certain margin into account. We used an exposure field of 10 kOe and a time of 1 ns for ATI.

3. Calculation Results

3.1 Improvement in writability

First, we discuss the improvement in writability.

Write-error (WE) and erasure-after-write (EAW)[14] are important factors in writability.

WE means that the magnetization does not switch to the recording direction during writing when the writing field $|H_w|$ magnitude is relatively small. WE decreases as the $|H_w|$ magnitude increases. On the other hand, EAW means that when the $|H_w|$ magnitude is too large, some dot magnetizations are reversed in the opposite direction to the recording direction caused by changing the $|H_w|$ direction after writing. WE and EAW are in a trade-off relationship in terms of the $|H_w|$ magnitude.

The improvement in writability is restricted to 10 years of archiving and ATI.

(1) Information stability during 10 years of archiving is determined by $K_{\beta0}$

$$K_{\beta0} = \frac{K_{ueff}V}{kT}, \tag{8}$$

and N is given by

$$N_0 = f_{\alpha0} \exp(-K_{\beta0}), \tag{9}$$

where $f_{\alpha0}$ is for $|H_w|$ = 0. There are two cases as regards $K_{\beta0}$, namely combinations of

(a) large K_{ueff} and small $V = D_m^2 h$ values, and

(b) small K_{ueff} and large V values.

(2) The ATI problem is equivalent to EAW, since ATI means writing in the adjacent track. Since WE and EAW are in a trade-off relationship, the better the WE is, the worse the ATI becomes and vice versa. A large V value is also needed for decreasing ATI when we choose a small K_{ueff} value.

If the K_{ueff} value, namely the H_{keff} value, is reduced, the $K_{\beta-}$ value in Eq. (4) decreases even for the same $K_{ueff}V$ value. This is advantageous to WE since the N_- value becomes large during writing and is disadvantageous to EAW since the N_- value also

becomes large at the end of writing. WE and EAW are in a trade-off relationship in terms of the K_{ueff} value even for the same $K_{\mathrm{ueff}}V$ value.

In addition, if the K_{ueff} value, namely the H_{keff} value, is reduced, the $K_{\beta+}$ value in Eq. (6) increases even for the same $K_{\mathrm{ueff}}V$ value. This is advantageous to WE since the N_+ value becomes small during writing.

If the EAW problem can be solved, a small K_{ueff} value is advantageous for improving writability as mentioned above. A large V value, namely a large h value, is needed for a certain $K_{\mathrm{ueff}}V$ value when we choose a small K_{ueff} value. However, it is difficult to manufacture a medium with a large h/D_{m} value. We assumed the maximum h/D_{m} value to be about two.

In the following, we discuss these problems that arise when we choose large and small K_{ueff} values.

3.2 Large anisotropy constant

When taking account of 10 years of archiving and ATI only, we can choose a dot height of 3.0 nm for a medium with $K_{\mathrm{u}}/K_{\mathrm{bulk}}$ = 0.8. The h/D_{m} value was 0.48. However, when $K_{\mathrm{u}}/K_{\mathrm{bulk}}$ = 0.8, the bER value is high as shown in Fig. 2. We discuss the reason for this using our calculation.

The N value is equal to the product of f_α and $\exp(-K_\beta)$. Figure 3 (a) shows the f_α value as a function of the writing time, where the writing field magnitudes $|H_{\mathrm{w}}|$ are 0 and 10 kOe. The medium temperature is also shown. At a time of zero, the medium temperature is T_{cm} and the writing field direction changes from downward to upward, and at a time of 1.27 ns, from upward to downward. A writing time determined by field is 1.27 ns.

The attempt frequency f_α (1/ns) is interpreted as the attempt number per nanosecond for dot magnetization reversal. Unfortunately, the f_α value becomes zero at T_{c}. Furthermore, the $f_{\alpha-}$ value for the dot magnetization reversal in the recording direction becomes small by $|H_{\mathrm{w}}|$.

The Boltzmann factor $\exp(-K_\beta)$ as shown in Fig. 3 (b) is interpreted as the dot magnetization reversal probability for each attempt, where the probability is equal to one when ϕ = 180 deg and $|H_{\mathrm{w}}| > H_{\mathrm{keff}}$. The probability decreases rapidly as the temperature decreases.

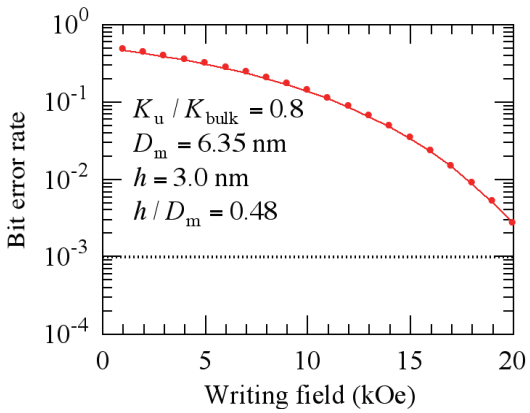

Fig. 2 Writing field $|H_{\mathrm{w}}|$ dependence of bit error rate for a $K_{\mathrm{u}}/K_{\mathrm{bulk}}$ value of 0.8.

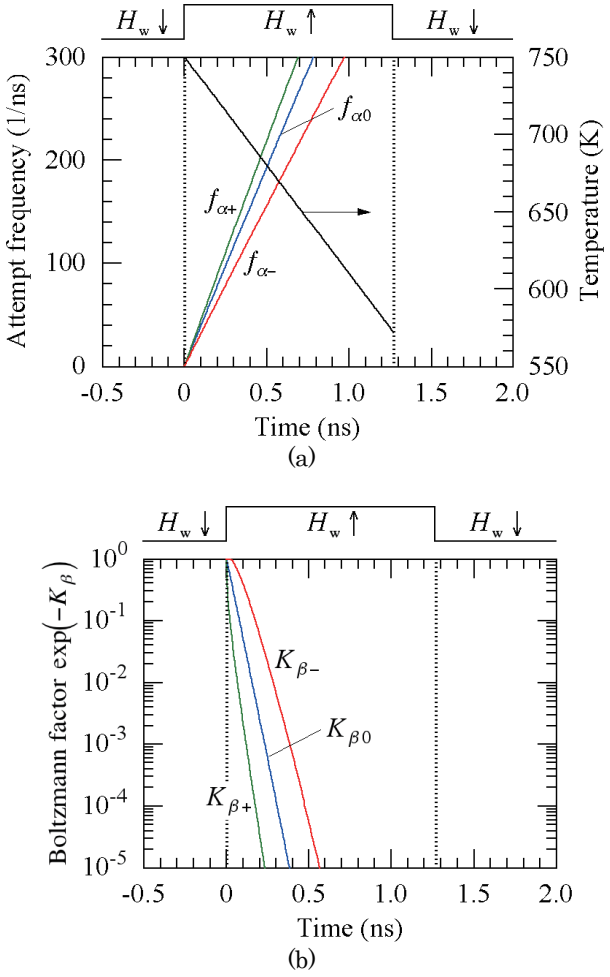

Fig. 3 (a) Attempt frequency f_α and medium temperature, and (b) Boltzmann factor $\exp(-K_\beta)$ as a function of writing time for a $K_{\mathrm{u}}/K_{\mathrm{bulk}}$ value of 0.8, where the writing field magnitudes $|H_{\mathrm{w}}|$ are 0 and 10 kOe.

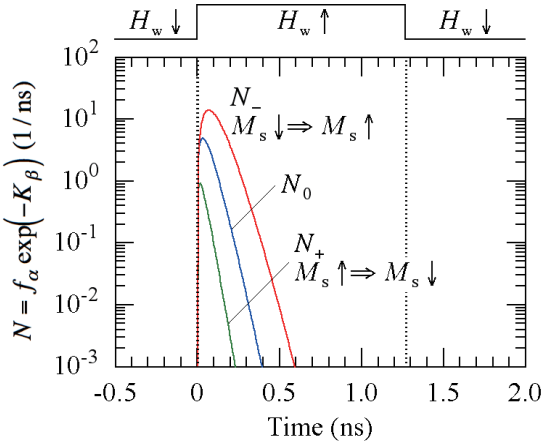

Fig. 4 Mean magnetization reversal number per nanosecond $N = f_\alpha \exp(-K_\beta)$ as a function of writing time for a $K_{\mathrm{u}}/K_{\mathrm{bulk}}$ value of 0.8, where the writing field magnitudes $|H_{\mathrm{w}}|$ are 0 and 10 kOe.

Figure 4 shows the $N = f_\alpha \exp(-K_\beta)$ value as a function of the writing time. The $N = f_\alpha \exp(-K_\beta)$ (1/ns) value is interpreted as the dot magnetization reversal number per nanosecond. The N_- value is the mean magnetization reversal number in the recording direction, and N_+ is that in the opposite direction to the recording direction.

When $|H_w| = 0$, the $N_0 = f_{\alpha 0} \exp(-K_{\beta 0})$ values in the recording and opposite directions are the same. As the $|H_w|$ value increases, the N_- value increases and the N_+ value decreases.

A medium with $K_u/K_{bulk} = 0.8$ has an N_+ value as shown in Fig. 4. This means that there is a situation where the magnetization reverses in the opposite direction to the recording direction.

Furthermore, the writing time determined by medium, where the N_- value is large, is much shorter than the writing time determined by field. For example, the writing time determined by medium, where the N_- value is larger than one per nanosecond, is 0.27 ns, and the writing time determined by field is 1.27 ns.

As a result, the bER value is high for a K_u/K_{bulk} value of 0.8.

3.3 Small anisotropy constant

Generally, a reduction in K_{ueff} is disadvantageous to EAW as mentioned above, since the N_- value becomes large at the end of writing time determined by field and the bER caused by EAW becomes large. However, the N_- value is extremely small at the end of the writing time for HDMR as shown in Fig. 4. Therefore, HDMR has a certain margin for EAW, since half of the writing time is for D_m and the rest is for Δ_D. Furthermore, HDMR also has a certain margin for the h/D_m value, namely 0.48, since the D_m value is relatively large, namely 6.35 nm. Therefore, the combination of small K_{ueff} and large V values is available for writability.

For a combination consisting of small K_{ueff} and large V values, 10 years of archiving and the ATI problem must be considered. The h value necessary for a bER of 10^{-3} after 10 years of archiving or AT writing increases as the K_u/K_{bulk} value decreases as shown in Fig. 5. The h/D_m value is 1.1 even for $K_u/K_{bulk} = 0.4$, since the D_m value of 6.35 nm is relatively large.

WE decreases and EAW increases as the $|H_w|$ magnitude increases. Figure 6 (a) shows that for a relatively small $|H_w|$ magnitude, the bER value, namely WE, decreases as the K_u/K_{bulk} value decreases where the h value was changed according to the result in Fig. 5. Although a large EAW can be seen for a

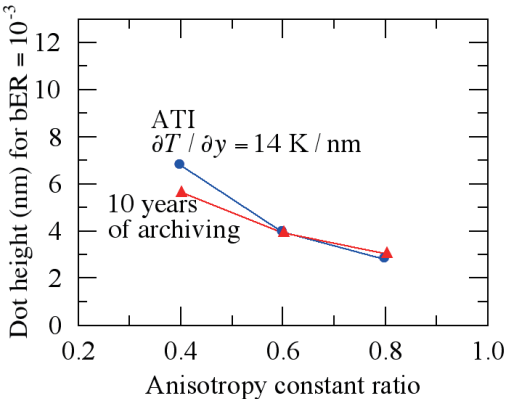

Fig. 5 Dot height h to achieve a bER of 10^{-3} as a function of the anisotropy constant ratio K_u/K_{bulk} after 10 years of archiving or AT writing.

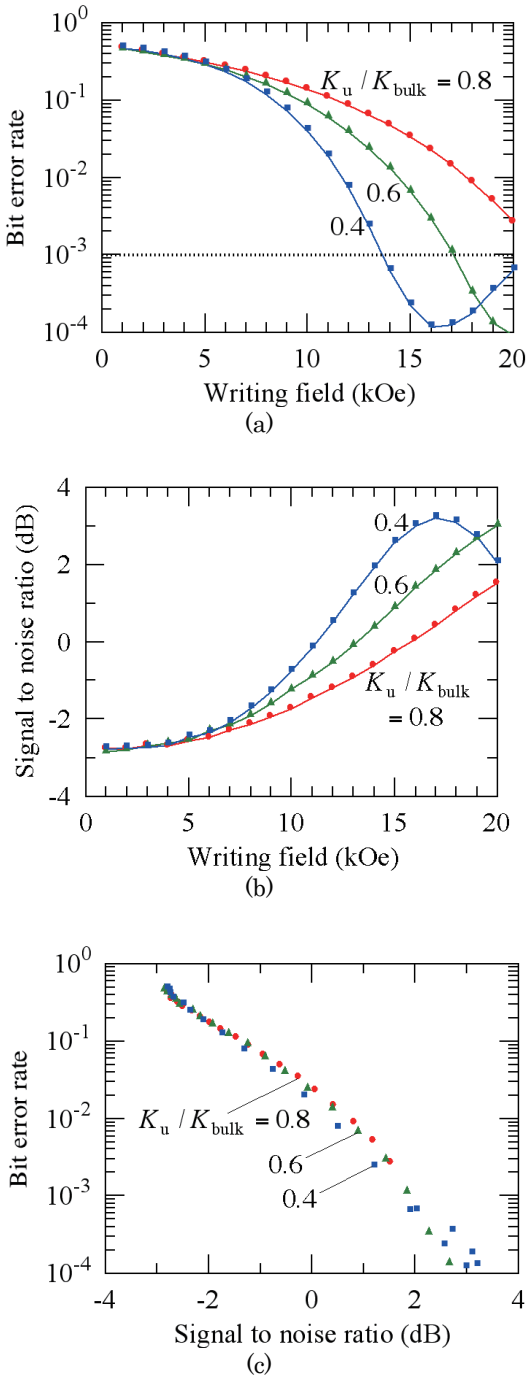

Fig. 6 Writing field $|H_w|$ dependence of (a) bit error rate (bER) and (b) signal to noise ratio (SNR) for various K_u/K_{bulk} values. (c) The bER value in (a) as a function of the SNR value in (b).

K_u/K_{bulk} value of 0.4 within the $|H_w|$ calculation range, it appears at a $|H_w|$ level exceeding about 16 kOe.

We confirmed the result in Fig. 6 (a) by employing a micromagnetic simulation. The calculation has already been reported in detail[5]. Figure 6 (b) shows the $|H_w|$ dependence of the signal to noise ratio (SNR) calculated employing the micromagnetic simulation, and Fig. 6 (c) shows the bER value in Fig. 6 (a) as a function of the SNR value in Fig. 6 (b). A good correlation can be seen between them. Therefore, our stochastic calculation in Fig. 6 (a) can almost entirely explain the result of the micromagnetic simulation in Fig. 6 (b).

When K_u/K_{bulk} = 0.4, the N_+ value is negligible as shown in Fig. 7, which can be compared with the result shown in Fig. 4 for K_u/K_{bulk} = 0.8. When K_u/K_{bulk} = 0.4, this means that there is almost no situation where the magnetization reverses direction compared with the recording direction. Furthermore, the writing time determined by medium of 0.35 ns for K_u/K_{bulk} = 0.4 is longer than that of 0.27 ns for K_u/K_{bulk} = 0.8. These mean that the recording is more guaranteed. Therefore, the bER caused by WE is low for a relatively small $|H_w|$ magnitude as shown in Fig. 6 (a).

We also confirmed the meaning of N_- and N_+ at $|H_w|$ = 10 kOe in Figs. 4 and 7 employing a micromagnetic simulator, EXAMAG LLG (Fujitsu Ltd.)[15], in which the Landau-Lifshitz-Gilbert (LLG) equation is solved by the finite-element method. The equivalent field for the energy of the thermal fluctuation was added. The dot size and magnetic property were the same with those in Figs. 4 and 7. The calculation step time was 10^{-16} s.

Figure 8 shows the time dependence of the magnetization z component M_z/M_s, which means the magnetization motion as a function of time. The calculation temperature was constant at 740 K, which corresponds to a time of 0.070 ns in Figs. 4 and 7. The N_- value shows the maximum at 0.070 ns as shown in Fig. 4. Since the thermal gradients and linear velocities are the same for Figs. 4 and 7, 740 K also corresponds to a time of 0.070 ns in Fig. 7. The initial magnetization and writing field directions are the $-z$ and z directions, respectively. The N_- and N_+ values are about 14 and 0.3 times per nanosecond, respectively, for K_u/K_{bulk} = 0.8 as shown in Fig. 4. It is expected that there will be 0.3 magnetization reversals in the opposite direction to the recording direction within 1 ns. As expected, several magnetization reversals can be observed within 10 ns as shown in Fig 8 (a). If we employ a definition stating that the magnetization is reversed when the M_z/M_s value reaches less than -0.9, the magnetization reversal number is 4 times for the example in Fig 8 (a).

On the other hand, the N_+ value is about 10^{-3} times per nanosecond for K_u/K_{bulk} = 0.4 as shown in Fig. 7. There is almost no occasion where the magnetization reverses in the opposite direction to the recording direction. Therefore, the magnetization reverses immediately in the recording direction after time 0, and maintains that direction as shown in Fig. 8 (b).

The stochastic calculation result is consistent with that employing a micromagnetic simulation. A feature of our stochastic calculation is that it is easy to grasp the physical implication of HAMR writing including HDMR, and the calculation time is short.

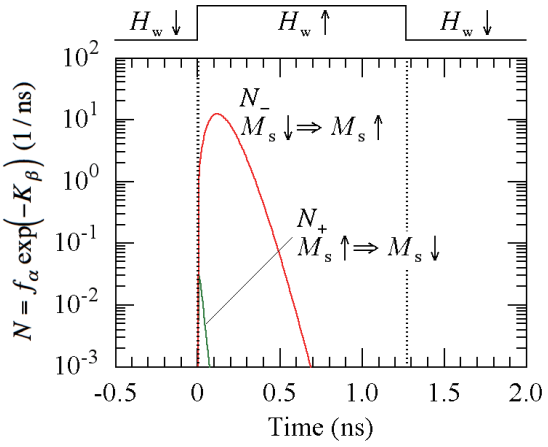

Fig. 7 Mean magnetization reversal number per nanosecond $N = f_\alpha \exp(-K_\beta)$ as a function of writing time for a K_u/K_{bulk} value of 0.4, where the writing field magnitude $|H_w|$ is 10 kOe.

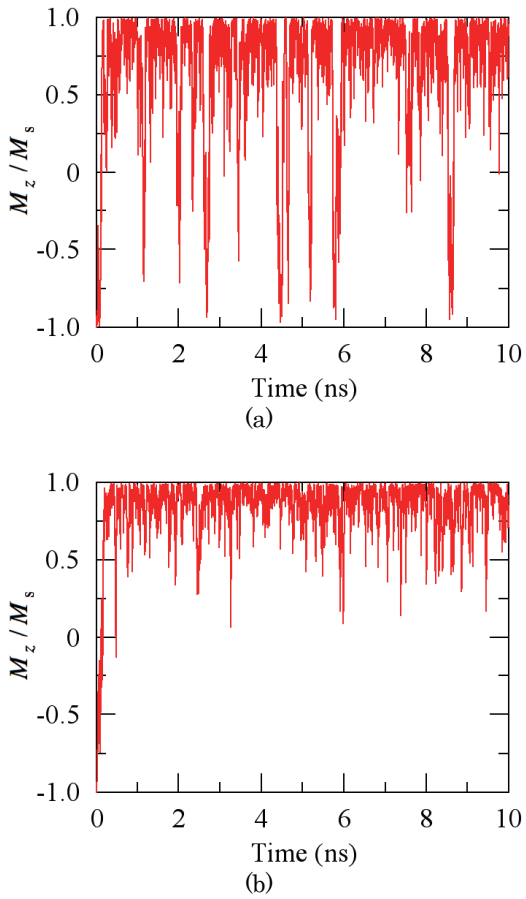

Fig. 8 Time dependence of magnetization z component M_z/M_s at 740 K for (a) K_u/K_{bulk} = 0.8 and (b) 0.4, where the writing field magnitude $|H_w|$ is 10 kOe.

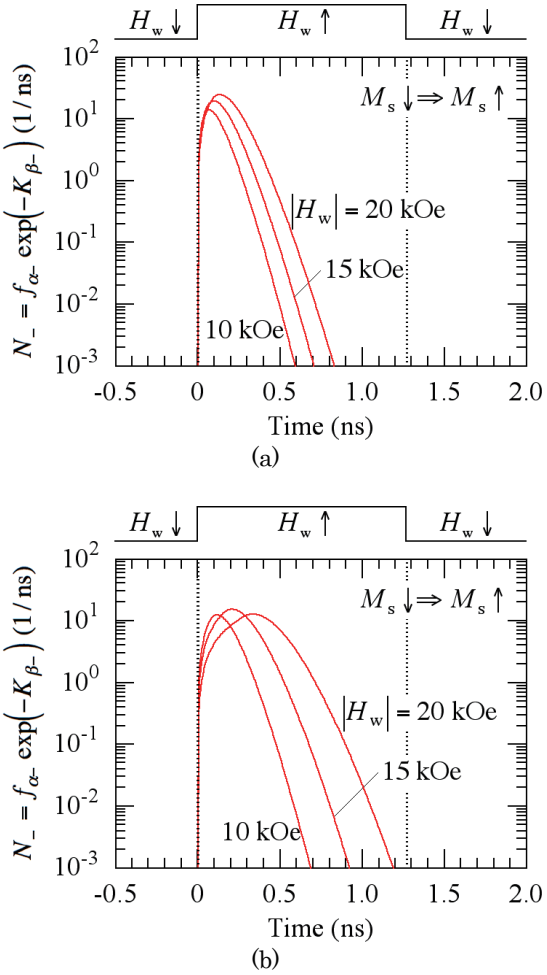

Fig. 9 Mean magnetization reversal number per nanosecond $N_- = f_{\alpha-}\exp(-K_{\beta-})$ as a function of writing time for various $|H_w|$ values. (a) K_u/K_{bulk} = 0.8 and (b) 0.4.

When K_u/K_{bulk} = 0.4, the bER caused by EAW is high for a relatively large $|H_w|$ magnitude as shown in Fig. 6 (a). When the $|H_w|$ value is large, for example 20 kOe, the N_- value is large at the end of the writing time determined by field as shown in Fig. 9 (b) for K_u/K_{bulk} = 0.4, which can be compared with the result shown in Fig. 9 (a) for K_u/K_{bulk} = 0.8. If a K_u/K_{bulk} value, namely if the H_{keff} value is small, the $K_{\beta-}$ value is also small as seen in Eq. (4) even for the same $K_{ueff}V$ value.

4. Conclusions

We examined the influence of the anisotropy constant on writability, taking account of 10 years of archiving and adjacent track interference in 4 Tbpsi shingled heated-dot magnetic recording (HDMR).

HDMR has a certain margin for erasure-after-write since the nonmagnetic spacing is large, and a certain margin for the dot aspect ratio since the dot size is relatively large. Therefore, the combination of a small anisotropy constant and a large dot volume can be used to improve write-error.

When we chose a small anisotropy constant, the bit error rate caused by write-error is low for a relatively small writing field magnitude.

However, the bit error rate caused by erasure-after-write is high for a relatively large writing field region.

Overall, a small anisotropy constant is effective in terms of obtaining a low bit error rate in HDMR.

Acknowledgement We acknowledge the support of the Advanced Storage Research Consortium (ASRC), Japan.

References

1) S. H. Charap, P. -L. Lu, and Y. He: *IEEE Trans. Magn.*, **33**, 978 (1997).
2) F. Akagi, M. Mukoh, M. Mochizuki, J. Ushiyama, T. Matsumoto, and H. Miyamoto: *J. Magn. Magn. Mater.*, **324**, 309 (2012).
3) F. Akagi, Y. Sakamoto, and N. Matsushima: 2021 IEEE International Magnetic Conference (INTERMAG), 2100043 (2021). DOI: 10.1109/INTERMAG42984.2021.9580007
4) K. Maeda and F. Akagi: *T. Magn. Soc. Jpn.* (Special Issues) (in Japanese), **7**, 1 (2023).
5) T. Kobayashi, Y. Nakatani, and Y. Fujiwara: *J. Magn. Soc. Jpn.*, **47**, 1 (2023).
6) T. Kobayashi, Y. Isowaki, and Y. Fujiwara: *J. Magn. Soc. Jpn.*, **39**, 8 (2015).
7) T. Kobayashi, Y. Nakatani, and Y. Fujiwara: *J. Magn. Soc. Jpn.*, **42**, 110 (2018).
8) T. Kobayashi and Y. Nakatani: *J. Magn. Soc. Jpn.*, **47**, 57 (2023).
9) M. Mansuripur and M. F. Ruane: *IEEE Trans. Magn.*, **MAG-22**, 33 (1986).
10) J. -U. Thiele, K. R. Coffey, M. F. Toney, J. A. Hedstrom, and A. J. Kellock: *J. Appl. Phys.*, **91**, 6595 (2002).
11) T. Kobayashi and I. Tagawa: *J. Magn. Soc. Jpn.*, **48**, 40 (2024).
12) T. Kobayashi and I. Tagawa: *J. Magn. Soc. Jpn.*, **47**, 128 (2023).
13) E. D. Boerner and H. N. Bertram: *IEEE Trans. Magn.*, **34**, 1678 (1998).
14) J. -G. Zhu and H. Li: *IEEE Trans. Magn.*, **49**, 765 (2013).
15) Fujitsu Release: *New Version of EXAMAG LLG Simulator*, https://www.fujitsu.com/global/about/resources/news/press-releases/2015/0324-01.html (2015).

Received Apr. 16, 2024; Accepted Jun. 18, 2024

J. Magn. Soc. Jpn., **48**, 88-93 (2024) <Paper>

Synthesis and high-field magnetic measurement of $Ba_2Sn_{2+x}Me_{1+x}Fe_{10-2x}O_{22}$

H. Harasawa, H. Mitamura*, M. Tokunaga*, K. Kakizaki, and K. Kamishima
Graduate School of Science and Engineering, Saitama Univ., *255 Shimo-okubo, Saitama 338-8570, Japan*
*Institute for Solid State Physics, Univ. of Tokyo, *Kashiwanoha 5-1-5, Kashiwa 277-8581, Japan*

We report the successful synthesis of $Ba_2Sn_{2+x}Me_{1+x}Fe_{10-2x}O_{22}$, a series of single-phase materials derived by substituting divalent metals (Me^{2+}=Ni^{2+}, Co^{2+}, Zn^{2+}, Mg^{2+}, and Cu^{2+}) into the $Ba_2Sn_2MeFe_{10}O_{22}$ layered structure. High-field magnetization measurements of the parent compound ($Ba_2Sn_2MeFe_{10}O_{22}$) unveil a unique magnetic response, marked by a plateau at high fields, indicating a field-induced alignment of moments near barium cations. This alignment contrasts with the antiferromagnetic arrangement of magnetic moments observed at low fields in a previous neutron diffraction study. The decrease in magnetization with substitution suggests the absence of the preference of Sn^{4+} for down-spin sites. This work paves the way for further exploration of the magnetic properties of $Ba_2Sn_2MeFe_{10}O_{22}$ and its derivatives.

Keywords: QS-type ferrite, $Ba_2Sn_{2+x}Me_{1+x}Fe_{10-2x}O_{22}$, phase diagram, pulsed high magnetic fields

1. Introduction

In the field of materials science, hexaferrites stand out due to their extensive historical significance and practical applications.[1-3] They are primarily oxides with iron acting as the principal magnetic ion, typically in the high-spin Fe^{3+} state. Additionally, these materials contain alkaline earth ions, such as Ba^{2+} or Sr^{2+}, which characterizes distinct structural units in hexaferrites. The composite structure of hexaferrite arises from combining fundamental structural units.[4-5] This layered configuration induces magnetic anisotropy, a critical factor influencing numerous physical properties. Typically, magnetic moments align perpendicular to the hexagonal layers, but exceptions occur, especially with the presence of divalent transition metal ions such as Co^{2+}, where magnetic alignment takes place within the hexagonal plane.[1-3]

The most prevalent variation of hexaferrite is the M-type, represented by the general formula $AFe_{12}O_{19}$, where A signifies divalent alkaline earth ions, commonly Ba^{2+} or Sr^{2+}.[1-2] Recognized for its strong magnetic characteristics, M-type hexaferrite is widely employed as a hard magnetic material, distinguished by its relatively high coercivity and saturation magnetization. The Y-type hexaferrite also stands out as a significant structural variant, with the chemical formula $Ba_2Me_2Fe_{12}O_{22}$, where *Me* represents a divalent transition metal. The Y-type hexaferrite exhibits stacking arrangements comprising S-block $(Me^{2+}{}_2Fe_4O_8)^{0\pm}$ and T-block $(Ba_2Fe_8O_{14})^{0\pm}$ structures.[4-5] In these materials, magnetic moments align within the hexagonal plane, allowing for free rotation in the ab plane, thus giving them the characteristic of soft magnetic materials. Their unique properties make them valuable for applications requiring high-frequency (GHz) RF usage.[6-10]

There is another hexaferrite of the QS-type that shares a stacking structure similar to that of the Y-type.[11-14] The present investigation focuses on the QS-type hexaferrites, $Ba_2Sn_2MeFe_{10}O_{22}$, characterized by a layered arrangement consisting of alternating S-block $(Me^{2+}Fe_5O_8)^+$ and Q-block $(Ba_2Sn_2Fe_5O_{14})^-$. Table 1 provides an overview of the crystallographic unit cell details for the QS-type hexaferrite. Previous reports established the presence of two formula units (QSQS) within the magnetic unit cell of this material; the magnetic structure exhibits a *c*-axis twice the length of

Table 1 Overview of the crystallographic unit cell details for the QS-type hexaferrite. Each row describes the quantity of atoms within the unit cell, the corresponding atom block, their designated labels in Fig. 8, and their associated coordinates for $Ba_2Sn_2NiFe_{10}O_{22}$ in Ref. 13.

$Ba_2Sn_2MeFe_{10}O_{22}$ (Space Group $P\bar{3}m1$) (a=5.9218 Å, c=14.3064 Å at T=300 K for *Me*=Ni)						
Atom (site)	Number of atoms	Block	Label in Fig. 8	x	$y = 2x$	z
Ba	2	Q		1/3	2/3	0.4235
Tetr(1)	2	S	M2, M9, M11, M18	1/3	2/3	0.9547
Tetr(2)	2	Q	M5, M6, M14, M15	0	0	0.3743
Oct(1)	2	Q	M4, M7, M13, M16	1/3	2/3	0.6789
Oct(2)	1	S	M1, M10	0	0	0
Oct(3)	6 (=3+3)	Q-S	M3, M8, M12, M17	0.1696	0.3392	0.1725
O(1)	2	Q		0	0	0.2393
O(2)	2	S		1/3	2/3	0.0890
O(3)	6	S		0.1572	0.3144	0.9145
O(4)	6	Q		0.4956	0.9912	0.2449
O(5)	6	Q		0.1752	0.3504	0.5912

Corresponding author: K. Kamishima (e-mail: kamisima@mail.saitama-u.ac.jp).

the crystallographic *c*-axis while sharing the same *a*-axis. As depicted in Fig. 8(b) later, the magnetic unit cell comprises 18 sites labeled along the *c*-axis. The magnetic moments associated with one formula unit (QS) exhibit equivalence and antiparallel alignment, leading to antiferromagnetism.[13] Despite its existence, $Ba_2Sn_2MeFe_{10}O_{22}$ has yet to be extensively investigated in determining whether the reported microscopic antiferromagnetic structure adequately accounts for macroscopic magnetization.

This study aims to explain the consequences of substituting $2Fe^{3+}$ with Sn^{4+} and Me^{2+} in $Ba_2Sn_2MeFe_{10}O_{22}$ for the following systems: Me^{2+}=Ni^{2+}, Co^{2+}, Zn^{2+}, Mg^{2+}, and Cu^{2+}. Introducing non-magnetic Sn^{4+} ions is anticipated to diminish the down-spin population, potentially inducing ferrimagnetism. To check the result of the arrangements of these magnetic moments, we examined the magnetization of the substituted samples, $Ba_2Sn_{2+x}Me_{1+x}Fe_{10-2x}O_{22}$, up to a high magnetic field of about 600 kOe. This method offers valuable insights into how magnetic moments are arranged, as demonstrated in a previous study involving a different type of substituted hexaferrite.[15]

2. Experimental Procedure

The preparation of the experimental materials involved the precise weighing of $BaCO_3$, α-Fe_2O_3, SnO_2, and *Me*O powders to achieve a targeted composition of $Ba_2Sn_{2+x}Me_{1+x}Fe_{10-2x}O_{22}$ ($-1.0 \le x \le 2.0$). The subsequent mixing process used a wet ball mill for 24 hours, followed by drying. The mixed powders were then shaped into disc-shaped samples with a diameter of 12 mm. The final step involved sintering the molded samples in air at temperatures between 1000°C and 1300°C for five hours. The crystal structure was investigated by powder X-ray diffraction (XRD) with Cu-Kα radiation (1.5405 Å). The extraction of lattice constants from the acquired X-ray diffraction peaks relied on Cohen's method of least-squares.[16] The magnetization measurements were carried out under various magnetic field strengths: up to 15 kOe by a VSM, up to 70 kOe by a SQUID, and up to 600 kOe by a pulsed magnetic field. Magnetization measurements in pulsed high magnetic fields utilized an induction method.

3. Experimental results and discussions

Figure 1 presents the X-ray diffraction (XRD) patterns of $Ba_2Sn_{2+x}Ni_{1+x}Fe_{10-2x}O_{22}$ series ($-1.0 \le x \le 2.0$) sintered at 1300°C. While a single phase was observed for compositions within the range of $-0.1 \le x \le 1.0$ at 1200°C, shifting *x* negatively led to the formation of the QS structure associated with $BaSn_{0.9}Fe_{5.47}O_{11}$. Conversely, increasing *x* resulted in forming the Sn oxide with the R block, identified as $BaSn_2Fe_4O_{11}$. This phenomenon is attributed to the formation of $BaSn_2Fe_4O_{11}$, which shares a composition close to $Ba_2Sn_4Ni_3Fe_6O_{22}$ (x = 2.0) upon reaching the cation substitution limit for the QS block.

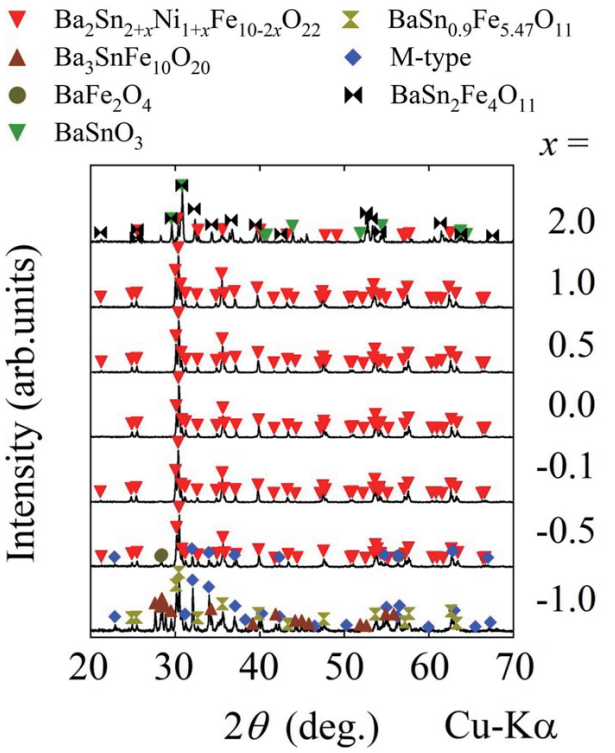

Fig. 1 X-ray diffraction (XRD) patterns of $Ba_2Sn_{2+x}Ni_{1+x}Fe_{10-2x}O_{22}$ series ($-1.0 \le x \le 2.0$) sintered at 1300°C.

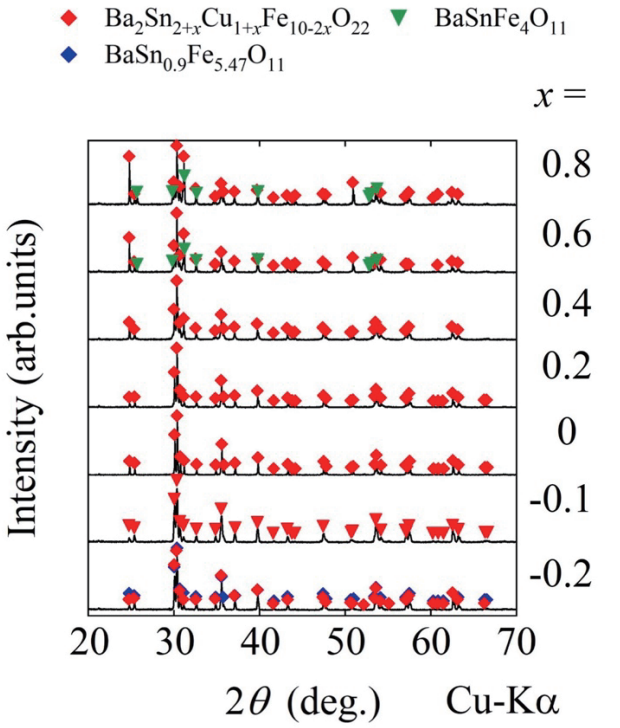

Fig. 2 X-ray diffraction patterns of $Ba_2Sn_{2+x}Cu_{1+x}Fe_{10-2x}O_{22}$ series ($-0.2 \le x \le 0.8$) sintered at 1200°C.

Figure 2 shows the X-ray diffraction patterns of $Ba_2Sn_{2+x}Cu_{1+x}Fe_{10-2x}O_{22}$ series ($-0.2 \le x \le 0.8$) sintered at

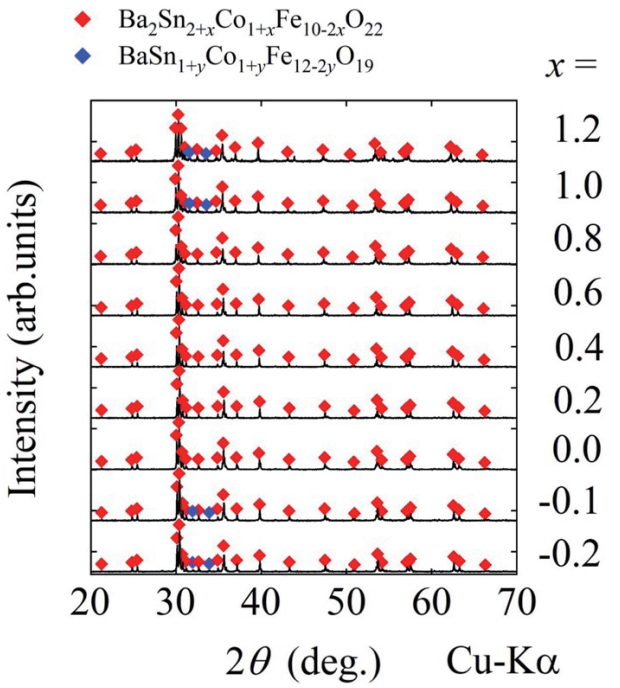

Fig. 3 X-ray diffraction (XRD) patterns of the $Ba_2Sn_{2+x}Co_{1+x}Fe_{10-2x}O_{22}$ series ($-0.2 \leq x \leq 1.2$) sintered at 1200°C.

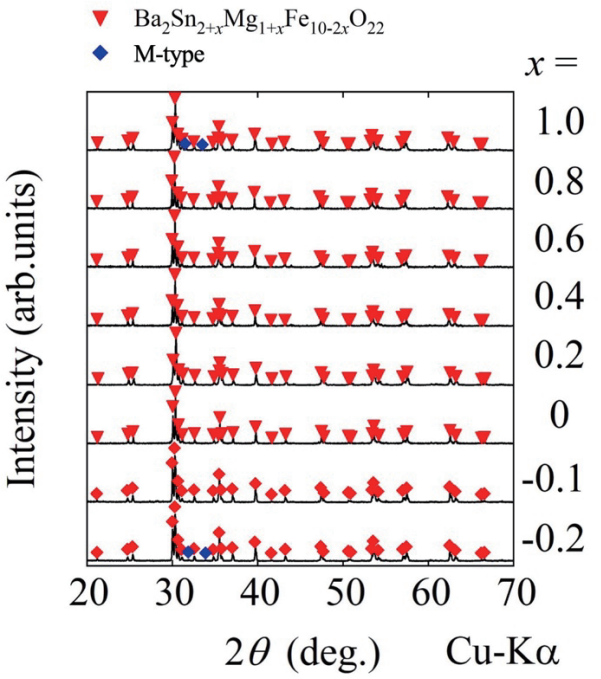

Fig. 4 X-ray diffraction (XRD) patterns of $Ba_2Sn_{2+x}Mg_{1+x}Fe_{10-2x}O_{22}$ series ($-0.2 \leq x \leq 1.0$) sintered at 1300°C.

1200°C. The analysis reveals the formation of a single phase for the composition range $-0.1 \leq x \leq 0.4$. However, samples with x values of 0.6, 0.8, and 1.0 undergo melting, preventing the achievement of a single phase in these cases.

Figure 3 shows the X-ray diffraction (XRD) patterns of $Ba_2Sn_{2+x}Co_{1+x}Fe_{10-2x}O_{22}$ series ($-0.2 \leq x \leq 1.2$) sintered at 1200°C. While a single phase was obtained for compositions within the range of $0 \leq x \leq 0.8$, the M-type hexaferrite was formed at both the substitution limits of $x = -0.1$ and 1.0. Although the minority phase is the same M-type hexaferrite, it is highly possible that the M-type hexaferrite in the sample at $x = -0.1$ contains more Fe^{3+} and less Me^{2+} and Sn^{4+} than at $x = 1.0$.

Figure 4 illustrates the X-ray diffraction (XRD) patterns of $Ba_2Sn_{2+x}Mg_{1+x}Fe_{10-2x}O_{22}$ series ($-0.2 \leq x \leq 1.0$) sintered at 1300°C. Similar to Fig. 3, a single phase was observed for compositions within the range of $-0.1 \leq x \leq 0.8$. The M-type hexaferrite phase was again observed at the substitution limits, $x = -0.2$ and 1.0.

Figure 5 shows the X-ray diffraction patterns of $Ba_2Sn_{2+x}Zn_{1+x}Fe_{10-2x}O_{22}$ series ($-0.2 \leq x \leq 1.0$) sintered at 1300°C. Similar to the observations in Figure 3, analysis of the patterns reveals the formation of a single phase for the composition range $-0.1 \leq x \leq 0.6$. Additionally, the M-type phase was observed at both the substitution limits, $x = -0.2$ and 1.0.

Figure 6 depicts a schematic diagram representing the single-phase fabrication range for the $Ba_2Sn_{2+x}Me_{1+x}Fe_{10-2x}O_{22}$ series (where Me^{2+}=Ni^{2+}, Co^{2+}, Zn^{2+}, Mg^{2+}, and Cu^{2+}). This diagram is based on the analysis of X-ray diffraction (XRD) patterns obtained from samples sintered at temperatures ranging from 1100°C to 1300°C and containing varying x values within the range of $-0.2 \leq x \leq 1.2$.

Figure 7 shows the magnetization curves of $Ba_2Sn_2MeFe_{10}O_{22}$ (Me^{2+}=Ni^{2+}, Co^{2+}, Zn^{2+}, Mg^{2+}, and Cu^{2+}) and the Fe^{3+} system $Ba_2Sn_{1.8}Fe_{10.94}O_{22}$ (=

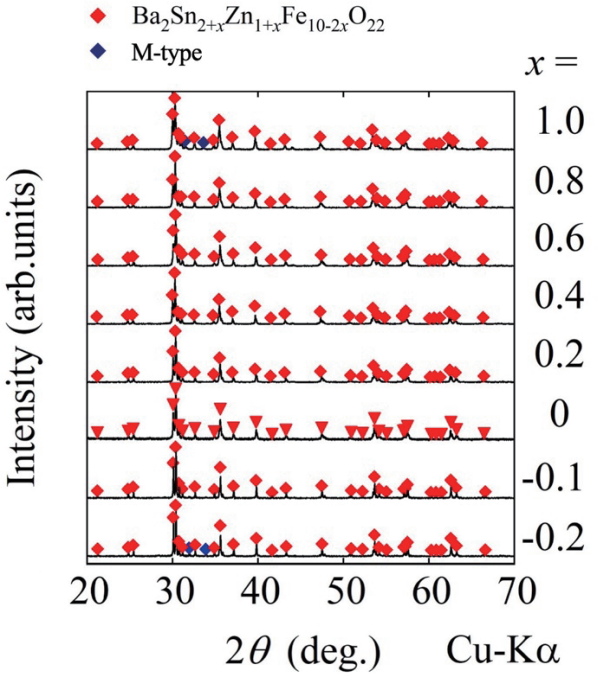

Fig. 5 X-ray diffraction patterns of $Ba_2Sn_{2+x}Zn_{1+x}Fe_{10-2x}O_{22}$ series ($-0.2 \leq x \leq 1.0$) sintered at 1300°C.

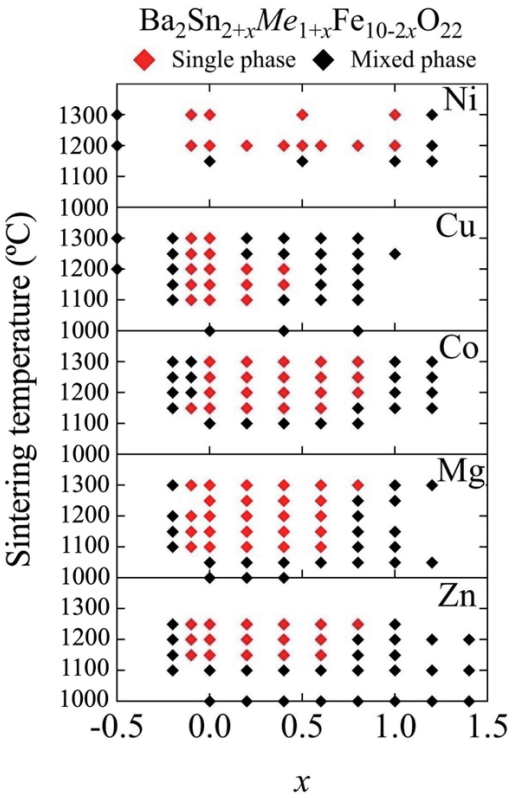

Fig. 6 Schematic diagram representing single-phase fabrication range for $Ba_2Sn_{2+x}Me_{1+x}Fe_{10-2x}O_{22}$ series (where Me^{2+}=Ni^{2+}, Co^{2+}, Zn^{2+}, Mg^{2+}, and Cu^{2+}).

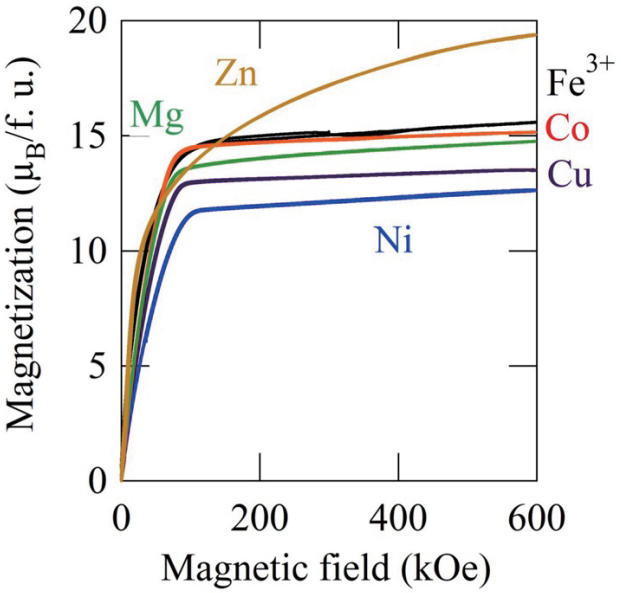

Fig. 7 Magnetization curves of $Ba_2Sn_2MeFe_{10}O_{22}$ (Me^{2+}=Ni^{2+}, Co^{2+}, Zn^{2+}, Mg^{2+}, and Cu^{2+}) and Fe^{3+} system $Ba_2Sn_{1.8}Fe_{10.94}O_{22}$ (= $2BaSn_{0.9}Fe_{5.47}O_{11}$), measured at T=4.2 K up to H=600 kOe.

$2BaSn_{0.9}Fe_{5.47}O_{11}$), measured at T=4.2 K up to H=600 kOe. The magnetization curve of the Zn-based QS-type hexaferrite did not reach full saturation, contrasting with QS-type hexaferrites containing alternative divalent cations. Zn^{2+} ions predominantly occupy tetrahedral sites, specifically M2, M9, M11, and M18, within the S blocks of the QS-type unit cell, which features alternating Q-, S-, Q-, and S-blocks. Notably, these tetrahedral sites within the S block serve as bottlenecks for transition metal ions when traced along the block stacking direction. The presence of non-magnetic Zn ions at these bottleneck positions can significantly disrupt the exchange interaction, hindering magnetization saturation compared to that observed in QS-type hexaferrites with different cations.

The figure demonstrates that the high-field magnetization at H=600 kOe approaches a value of 20 μB/f.u. for the Zn-system, 15 μB/f.u. for the Mg, Co, and Fe systems, and 13 μB/f.u. for the Cu and Ni systems. While generally in agreement with the findings of M. C. Cadée *et al.* up to 400 kOe, our results present some noticeable discrepancies. These differences likely stem from variations in sample synthesis conditions, particularly our approach compared to that of Cadée's, who subjected samples to sintering at 1197°C over several days. Such differences may induce alterations in ionic distribution and, consequently, magnetic properties, as demonstrated in the case of $MgFe_2O_4$.[17] Notably, the magnetization curves exhibit a kink-like feature up to an applied field of 600 kOe. These observations allow us to discuss the magnetic structure at H=600 kOe.

Figure 8 depicts the (a) two crystallographic unit cells and (b) magnetic unit cell proposed by M. C. Cadée *et al.*[13] Their analysis suggests that the cancellation of ionic magnetic moments within the magnetic unit cell leads to antiferromagnetic behavior. Our present work investigates whether this spin configuration can account for the observed magnetization at the plateau.

Considering the Zn-system as an example, the replacement of non-magnetic Sn^{4+} and Zn^{2+} ions with 2 Fe^{3+} ions in two chemical formula units results in a distribution of 20 Fe^{3+} magnetic moments. To achieve agreement with the experimental value of 20 μB/f.u.,

$$2 \times (7 \times 5 - 3 \times 5) = 40\ \mu_B \quad (1)$$

must be satisfied. This means that the two-chemical-formula-unit magnetic structure exhibits fourteen right-pointing and six left-pointing magnetic moments. Based on their valences and coordination preferences, we propose a plausible configuration (Fig. 8(c)) where Sn^{4+} ions occupy M8 and M12 sites, and Zn^{2+} ions occupy M2 and M18 sites. However, this configuration yields a magnetic moment of 30 μB per unit cell, which is inconsistent with the observed 40 μB plateau magnetization.

The inability of the spin configuration proposed by M. C. Cadée *et al.* to account for the observed plateau magnetization necessitates a re-evaluation of the magnetic structure. While the bond length between M5 and M6 in Fig. 8(b) is significantly long, the corresponding bond angle is 76°, as shown in Fig. 8(d). This angle being close to 90° suggests a potential

ferromagnetic alignment of the magnetic moments.

So, we propose a field-induced alignment of moments near barium cations in the Q-block. Figure 8(e) depicts this magnetic structure with aligned magnetic moments at the M5-M6 and M14-M15 sites, while other sites maintain antiparallel alignments, as in Fig. 8(b). In other words, the directions of magnetic moments at the M6-M14 sites in Fig. 8(d) oppose those in Fig. 8(b). This configuration results in a distribution of eighteen right-pointing and eight left-pointing magnetic moments per unit cell, leading to a ferrimagnetic arrangement throughout the crystal. Based on considering the local charge balance, Sn^{4+} and Zn^{2+} are expected to occupy the positions indicated in Fig. 8(f).

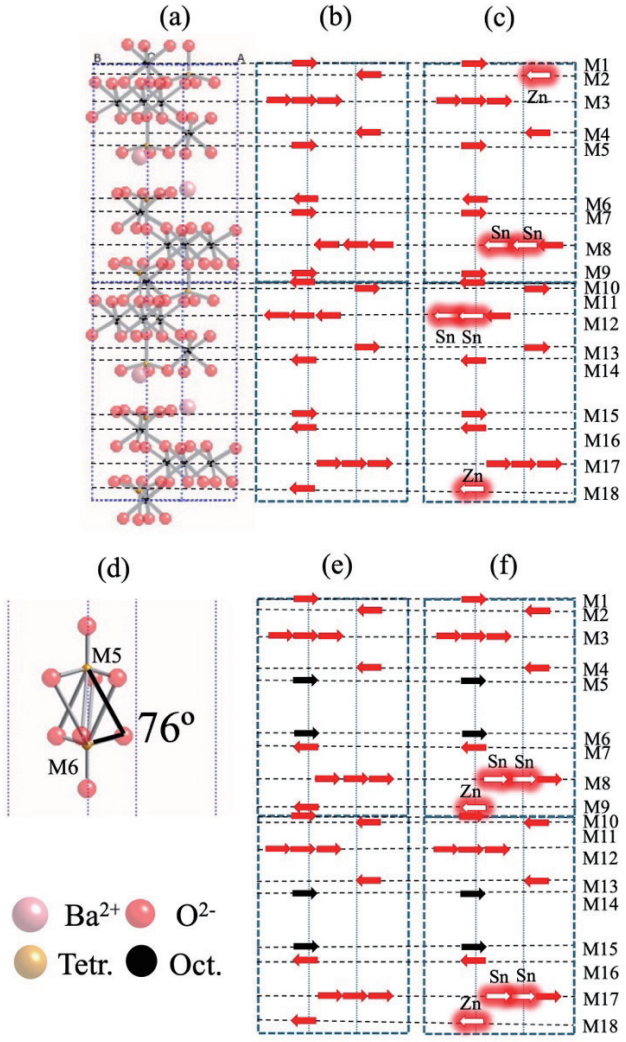

Fig. 8 (a) Two crystallographic unit cells of $Ba_2Sn_2MeFe_{10}O_{22}$, (b) magnetic structure of $Ba_2Sn_2MeFe_{10}O_{22}$ proposed by M. C. Cadée *et al.* (1986), (c) plausible spin configuration based on (b) with Sn^{4+} and Zn^{2+} cations, (d) bond between M5 and M6 in Q block, (e) modified magnetic structure with aligned magnetic moments at M5-M6 and M14-M15 sites, and (f) plausible spin configuration based on (e) with Sn^{4+} and Zn^{2+} cations.

Therefore, at low magnetic fields, the dominant magnetic structure is the one depicted in Fig. 8(b), which leads to the cancellation of the magnetic moments within the crystal. However, at high magnetic fields, the alignment of the M5-M6 and M14-M15 magnetic moments (as shown in Fig. 8(e)) gives rise to the observed plateau.

We consider if the magnetic structure shown in Fig. 8(e) applies to another divalent metal substitution. Considering the non-magnetic Mg-system, the same configuration as in Fig. 8(e) would yield 18 right-pointing and eight left-pointing moments. Replacing Fe^{3+} with four non-magnetic Sn^{4+} and two Mg^{2+} in the Mg system requires an equation of

$$2 \times (6.5 \times 5 - 3.5 \times 5) = 30\ \mu_B \quad (2)$$

for the experimental value of 15 μ_B/f.u. This translates to thirteen right-pointing and seven left-pointing moments. Assigning Sn^{4+} and Mg^{2+} to the Fig. 8(e) configuration, Sn^{4+} likely occupies M8 and M17 due to its high valence and preference for octahedral sites. Mg^{2+}, being able to occupy both tetrahedral and octahedral sites as the incomplete inverse spinel structure of $MgFe_2O_4$ demonstrates, is assumed to have a 50% occupancy in M1, M2, M10, and M11 of the S block.

Figure 9 shows the magnetization values of $Ba_2Sn_{2+x}Me_{1+x}Fe_{10-2x}O_{22}$ at an applied magnetic field of 550 kOe and a temperature of 4.2 K. The magnetization decreased with increasing substitution levels. This observed reduction can be attributed to two main factors: (1) the substituted ions, which possess smaller magnetic moments compared to Fe^{3+}, do not exhibit a preferential occupancy of the left-handed spin sites, and (2) the dilution of the system with non-magnetic Sn^{4+} ions, which disrupts the super-exchange interaction. It

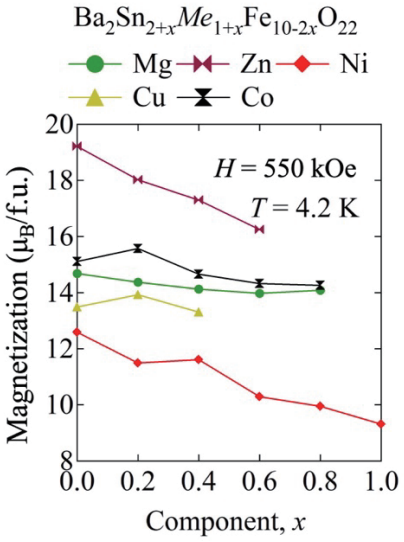

Fig. 9 Magnetization of $Ba_2Sn_{2+x}Me_{1+x}Fe_{10-2x}O_{22}$ at applied magnetic field of 550 kOe and temperature of 4.2 K.

is likely that introducing non-magnetic Sn^{4+} ions does not diminish the down-spin population.

4. Conclusion

We report the successful achievement of single-phase synthesis for the $Ba_2Sn_{2+x}Me_{1+x}Fe_{10-2x}O_{22}$ series, which represents a divalent metal substitution system derived from the $Ba_2Sn_2MeFe_{10}O_{22}$ QS-type hexagonal ferrite. This achievement was realized within specific synthesis temperature ranges (T_S) and substitution level ranges (x) for the Co, Ni, Mg, Zn, and Cu systems. Furthermore, the investigation of the magnetic properties of the $Ba_2Sn_2MeFe_{10}O_{22}$ ferrite suggests the following potential explanation: at low magnetic fields, the dominant magnetic structure, as described by M. C. Cadée *et al.*, leads to the cancellation of the magnetic moments within the unit cell. However, at high magnetic fields, the alignment of the magnetic moments near barium cations in the Q block results in the observed plateau. The magnetization of $Ba_2Sn_{2+x}Me_{1+x}Fe_{10-2x}O_{22}$ decreased with increasing substitution levels, which implies that introducing non-magnetic Sn^{4+} ions does not diminish the down-spin population.

Acknowledgements This work was supported by JSPS KAKENHI Grant Number 21K04862. The high-field magnetic measurements were carried out along the proposals No. 202211-HMBXX-0005 and 202209-HMBXX-0089, and partly supported by ISSP of the University of Tokyo.

References

1) R. C. Pullar: *Prog. Mater. Sci.*, **57**, 1191 (2012).
2) T. Kimura: *Annu. Rev. Condens. Matter Phys.*, **3**, 93 (2012).
3) U. Ozgur, Y. Alivov, and H. Morkoc: *J. Mater. Sci.: Mater. Electron.*, **20**, 789 (2009).
4) J. A. Kohn, D. W. Eckart, and C. F. Cook: *Science*, **172**, 519 (1971).
5) C. Delacotte, G. F. S. Whitehead, M. J. Pitcher, C. M. Robertson, P. M. Sharp, M. S. Dyer, J. Alaria, J. B. Claridge, G. R. Darling, D. R. Allan, G. Winter, and M. J. Rosseinsky: *IUCrJ*, **5**, 681 (2018).
6) Y. Bai, J. Zhou, Z. Gui, Z. Yue, and L. Li: *J. Magn. Magn. Mater.*, **264**, 44 (2003).
7) C. A. Stergiou and G. Litsardakis: *J. Magn. Magn. Mater.*, **405**, 54 (2016).
8) J. -H. You and S. -I. Yoo: *J. Magn. Magn. Mater.*, **471**, 255 (2019).
9) J. -H. You, S. Choi, S. -Y. Park, and S. I. Yoo: *J. Magn. Magn. Mater.*, **491**, 165640 (2019).
10) K. Zhai, N. Su, J. Sun, J. Cheng, Z. Liu, and Y. Sun: *J. Mater. Chem. C*, **7**, 4173 (2019).
11) M. C. Cadée and D. J. W. Ijdo: *J. Solid State Chem.*, **36**, 314 (1981).
12) M. C. Cadée and D. J. W. Ijdo: *J. Solid State Chem.*, **40**, 290 (1981).
13) M. C. Cadée, H. J. M. de Groot, L. J. de Jongh and D. J. W. Ijdo: *J. Magn. Magn.* Mater., **62**, 367 (1986).
14) F. Sandiumenge, S. Galí, R. Rodríguez-Clemente, X. Batlle, and X. Obradors: *J. Solid State Chem.*, **92**, 213 (1991).
15) K. Kamishima, A. Yonezawa, K. Kakizaki, A. Miyake, H. Mitamura, and M. Tokunaga: *J. Magn. Magn. Mater.*, **538**, 168251 (2021).
16) B. D. Cullity: *Elements of X-ray Diffraction*, 2nd ed., p. 359, 366 (Addison-Wesley, 1978).
17) H. O'Neill, H. Annersten, and D. Virgo: *Am. Mineral.*, 77, 725 (1992).

Received Apr. 3, 2024; Revised Apr. 29, 2024; Accepted May 29, 2024

Editorial Committee Members・Paper Committee Members

Notice for Photocopying

編集委員・論文委員

複写をされる方へ

Journal of the Magnetics Society of Japan

Vol. 48 No. 5 (通巻第335号) 2024年9月1日発行

Vol. 48 No. 5 Published Sep. 1, 2024
by the Magnetics Society of Japan
Tokyo YWCA building Rm207, 1–8–11 Kanda surugadai, Chiyoda-ku, Tokyo 101–0062
Tel. +81–3–5281–0106 Fax. +81–3–5281–0107

Printed by JP Corporation Co., Ltd.
Sports Plaza building 401, 2–4–3, Shinkamata Ota-ku, Tokyo 144–0054
Advertising agency: Kagaku Gijutsu-sha

発行：(公社)日本磁気学会 101–0062 東京都千代田区神田駿河台 1–8–11 東京YWCA会館 207 号室
製作：ジェイピーシー 144–0054 東京都大田区新蒲田 2–4–3 スポーツプラザビル401 Tel.（03）6715–7915
広告取扱い：科学技術社 111–0052 東京都台東区柳橋 2–10–8 武田ビル 4F Tel.（03）5809–1132